

Observation of flat bands and Dirac-like bands in a weakly correlated semimetal YRu_2Si_2

Anup Pradhan Sakhya,¹ Sabin Regmi,¹ Milo Sprague,¹ Mazharul Islam Mondal,¹ Iftakhar Bin Elius,¹ Nathan Valadez,¹ Andrzej Ptok,² Dariusz Kaczorowski,³ and Madhab Neupane^{1,*}

¹*Department of Physics, University of Central Florida, Orlando, Florida 32816, USA*

²*Institute of Nuclear Physics, Polish Academy of Sciences,*

W. E. Radzikowskiego 152, PL-31342 Kraków, Poland

³*Institute of Low Temperature and Structure Research,
Polish Academy of Sciences, ul. Okólna 2, 50-422 Wrocław, Poland*

(Dated: April 18, 2023)

Condensed matter systems with flat bands have been the center of research interest in recent years as they provide a platform for the emergence of exotic many-body states, such as superconductivity, ferromagnetism, and the fractional quantum Hall effect. However, realization of materials possessing flat bands near the Fermi level experimentally is very rare. Here, we report the experimental observation of flat bands in a weakly-correlated system YRu_2Si_2 employing angle-resolved photoemission spectroscopy (ARPES) which is supported by first-principles calculations. These flat bands originate from Ru d orbitals and are found to be sensitive to the polarization of light. In addition, ARPES data revealed surface and bulk Dirac-like bands. The observed ARPES data is in excellent agreement with the density functional theory results. The presence of both flat bands and Dirac-like bands in YRu_2Si_2 suggest a unique synergy of correlation and topology in this material belonging to the centrosymmetric tetragonal ThCr_2Si_2 -type structure thus establishing a new platform to investigate flat band physics in combination with non-trivial topological states in a weakly correlated system.

Introduction

Dirac materials with flat bands have attracted immense research interest in the material science community owing to its possibility of studying the interplay between topology and electron correlation [1]. Unlike the linear bands that possess massless quasiparticles, flat bands are dispersionless within a limited momentum range, usually hosting super-heavy localized electrons, extremely high density of states, and symmetry broken correlated states [2–4] such as superconductivity [5], ferromagnetism [6], Wigner crystallization [7], the fractional quantum Hall effect [8–13], giant anomalous Hall, and anomalous Nernst effects [14–17]. In the absence of time-reversal symmetry, a flat band can further acquire a nonzero Chern number as its topological invariant, leading to exotic topological matter such as Chern insulators and Weyl semimetals [18, 19]. The presence of a flat band in superconductors enhances the density of states at the Fermi level which can increase the coupling constant and the superconducting transition temperature [20, 21]. This mechanism has been used to understand the unexpected superconductivity in twisted graphene and rhombohedral graphite [22–24]. Additional examples of flat band materials include kagome lattices, where the destructive quantum interference due to the frustrated lattice geometry can lead to a flat band [25, 26]. Self-localization of the electron wave functions can be achieved in the kagome lattice, which is made up of interlaced triangles, by the destructive interference that occurs around each hexagon, resulting in a flat band with no dispersion [26, 27]. Flat bands in several kagome materials have been identified [20, 26, 28–31]. However, the measurements are challenging to conduct due to the complexity of the electronic structure in the photoemission data and the lack of momentum resolution in scanning tunneling spectroscopy [32]. In addition to these most of the materials have flat bands quite far away from the Fermi level which restricts its potential for further fundamental research and its usefulness in quantum devices [33, 34]. Flat bands have also been observed in rhombohedrally stacked trilayer graphene [21, 35–38], twisted bilayer graphene when the two layers are twisted relative to one another by a magic angle of 1.1° [39, 40], and in Cs-doped graphene [41]. However, these systems are prepared from exfoliated flakes which prevent their deterministic preparation in large volumes and also these are unstable as the two layers have to be rotated at certain angles [41].

Even though flat bands have been studied in kagome systems and artificially engineered 2D layers such as twisted graphenes, experimental observation of flat bands in weakly correlated systems is not realized. Here, we report the electronic structure of YRu_2Si_2 determined by combining angle-resolved photoemission spectroscopy (ARPES) and density functional theory (DFT) calculations. We report the experimental observation of flat bands around 170 meV extending over a large area of the Brillouin zone along with the presence of multiple Dirac-like bands in this material. The flat bands are reproduced from the DFT calculations, the 2D Dirac-like crossing is observed on the Y

* Corresponding author: madhab.neupane@ucf.edu

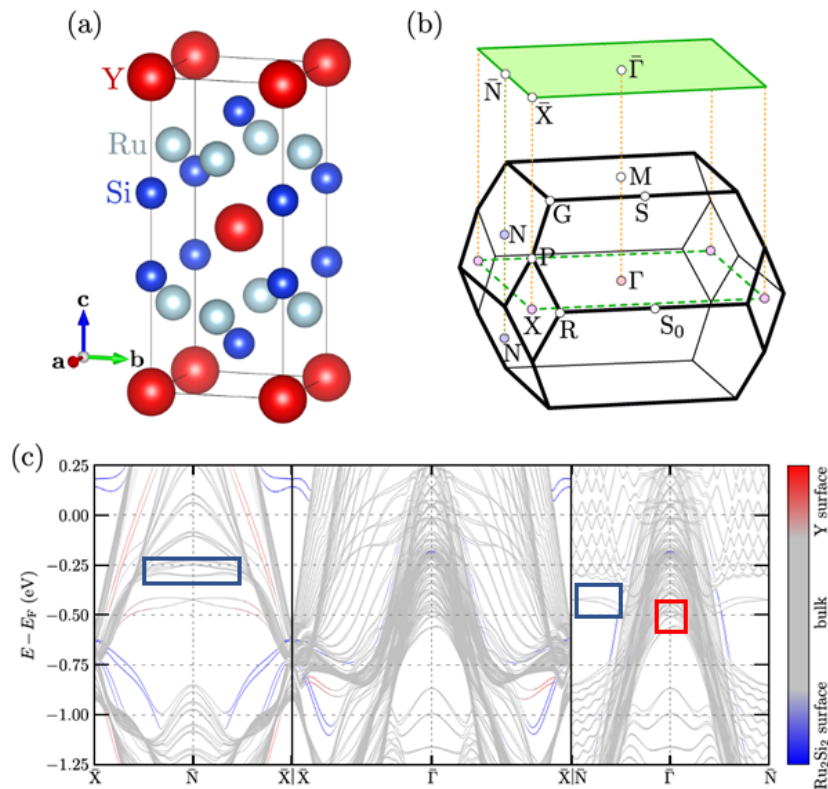


Fig. 1. Crystal structure and DFT calculations of YRu₂Si₂. **a** Crystal structure of YRu₂Si₂ where the red, aqua, and blue colored solid spheres denote the Y, Ru and Si atoms, respectively. **b** Bulk Brillouin zone and its projection on to the (001) surface BZ. High symmetry points are marked. **c** Slab calculations along the $\bar{X}-\bar{N}-\bar{X}$, $\bar{X}-\bar{\Gamma}-\bar{X}$, and $\bar{N}-\bar{\Gamma}-\bar{N}$ directions. The termination dependence of surface states is marked by colors (as labeled). The blue and red rectangles highlight the flat bands and the Dirac-like bands, respectively.

terminated surface at the \bar{X} point along with the presence of a bulk 3D Dirac-like band at the $\bar{\Gamma}$ point. Our work thus establishes this material as a unique platform to realize coexisting flat bands and Dirac-like bands in a system that is neither kagome based nor it has intrinsic $4f$ correlated states. YRu₂Si₂ belongs to the ThCr₂Si₂-type family of the general formula AT₂X₂ (and very often called 122 families). There are numerous elemental combinations for which the ThCr₂Si₂ derivatives exist. Alkali, alkaline earth, rare earth, or actinoid metals can make up the A cations, while the entire family of transition metals has been seen on the T sites [42]. The valence electron count, and consequently the magnetic ground states, can vary due to the flexibility in the site occupancies. In the context of heavy fermion systems, particularly the phases containing cerium and uranium, have received a great deal of attention during the past thirty years [42]. CeRu₂Si₂ is a well-known non-magnetic Kondo lattice compound with a high electronic specific heat coefficient of 350 mJ/K²·mol [43]. YRu₂Si₂ is an excellent reference compound without any $4f$ component.

Results

Crystal structure and DFT calculations. The crystal structure of YRu₂Si₂ is shown in Fig. 1a. The compound crystallizes in the ThCr₂Si₂-type body-centered tetragonal structure (I4/mmm, space group No. 139), with lattice constants $a = b = 4.1580(6)$ Å, and $c = 9.546(2)$ Å [42] (see Supplementary Note 1, Supplementary Fig. 1 and Supplementary Fig. 2 for details of crystal characterization). The primitive unit cell contains one Y atom at the $2a$ (0,0,0) Wyckoff position, two Ru atoms at $4d$ (0,1/2,1/4), and two Si atoms at $4e$ (0,0,0.3684) [42]. The crystal structure of this material is mainly formed by edge-sharing RuSi₄ tetrahedra layers in the x - y plane which is separated by Y atoms. In Fig. 1b, the bulk Brillouin zone (BZ) and its projection on the (001) surface is shown. In Fig. 1c, we present the slab calculations along the $\bar{X}-\bar{N}-\bar{X}$, $\bar{X}-\bar{\Gamma}-\bar{X}$, and $\bar{N}-\bar{\Gamma}-\bar{N}$ high-symmetry directions with the inclusion of spin-orbit coupling (SOC), which includes three time-reversal invariant momenta points. The grey bands represent the (001) surface projected bulk bands, red bands are the surface bands for Y termination and the blue bands are the surface states with Ru₂Si₂ surface termination. The calculated band structure exhibits multiple bands crossing the Fermi level (E_F) [44, 45] indicating YRu₂Si₂ to be a metal that is in accordance with the transport measurements (see Supplementary Fig. 1c). Hole-like bulk bands are seen around the $\bar{\Gamma}$ and the \bar{N} directions. Interestingly, we

$h\nu = 68$ eV, LH polarization

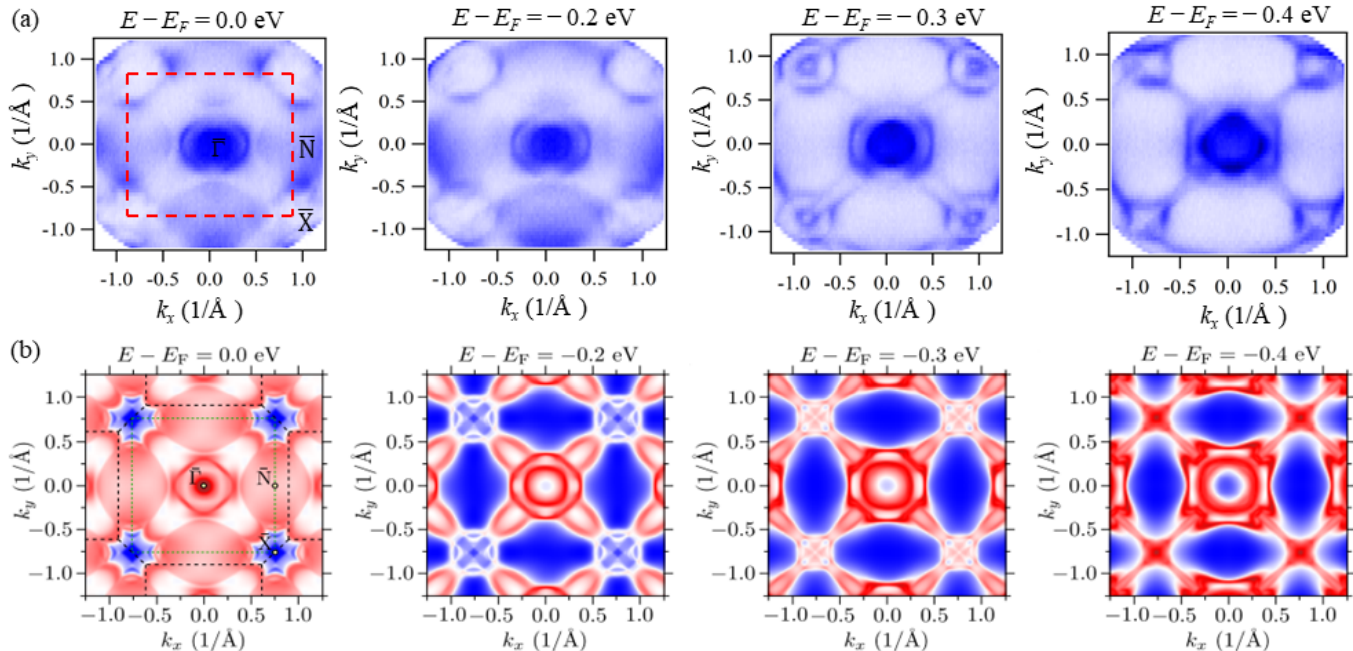


Fig. 2. Fermi surface and constant energy contours. **a** ARPES measured Fermi surface (first panel) and constant energy contours measured using a photon energy of 68 eV at various binding energies as indicated on top of each plot. **b** Respective Fermi surface and constant energy contours obtained from DFT calculations. The experimental data were taken at the SSRL beamline 5-2 at a temperature of 15 K using LH polarization.

observe flat bands that extends to a large momentum range at around 270 meV and 380 meV binding energy along the \bar{X} - \bar{N} - \bar{X} and the \bar{N} - $\bar{\Gamma}$ - \bar{N} directions, respectively. For the Y-terminated surface, a Dirac-like dispersion exists at around 650 meV below the Fermi level at the \bar{X} point and a bulk Dirac-like feature is observed at the $\bar{\Gamma}$ point at around 500 meV which makes the band structure of this material very interesting.

Fermi surface and constant energy contours. In order to reveal the electronic structure of YRu_2Si_2 , we have measured the Fermi surface (FS) and constant energy contours (CECs) at various binding energies using a photon energy of 68 eV as presented in Fig. 2. Experimental FS maps and CECs are presented in Fig. 2a and the DFT calculated FS and CECs are presented in Fig. 2b. Both experimental and theoretical FSs are provided with BZs marked with high-symmetry points. Multiple pockets are observed at the FS, which indicates the complex band structure of this material. We observe multiple circular-shaped pockets at the $\bar{\Gamma}$ point, an oval-shaped pocket at the \bar{N} point and a pocket at the \bar{X} point. The energy contours presented in the right hand side of Figs 2a and 2b delineate how the band dispersions evolve with binding energies. The energy pockets at the $\bar{\Gamma}$ and the \bar{N} points grow bigger with binding energy, indicating the hole-like nature of the bands whereas the pocket at the \bar{X} point decreases in size indicating the electron-like nature. Several bulk pockets appear at higher binding energies, which can be clearly visualized from the CEC plots at binding energies of 200 meV, 300 meV, and 400 meV. The experimental FS and the CECs of the material are quite well reproduced in the calculated plots shown in Fig. 2b. The exception of some pockets such as the rhombus pocket at the $\bar{\Gamma}$ point can be explained from the polarization dependence which can be seen from the polarization-dependent maps presented in Supplementary Note 2, Supplementary Fig. 3, and Supplementary Fig. 4.

Observation of flat bands and Dirac-like bands from ARPES. Next, in order to examine the details of the band structure, we present the ARPES measured dispersion maps along various high-symmetry directions as shown in Fig. 3. The measurements have been performed for a photon energy of 62 eV using both LH and LV polarization. Along the \bar{X} - \bar{N} - \bar{X} direction, as shown in Fig. 3(a,b), we observe multiple bands crossing the E_F . Interestingly, we observe flat bands around 170 meV along the \bar{X} - \bar{N} - \bar{X} direction along with Dirac-like band at the \bar{X} point which are marked by black arrows. The flat bands are intense when measured with LH polarization and strongly suppressed when measured with LV polarization. Another hole-like band at around 800 meV is very sensitive to polarization

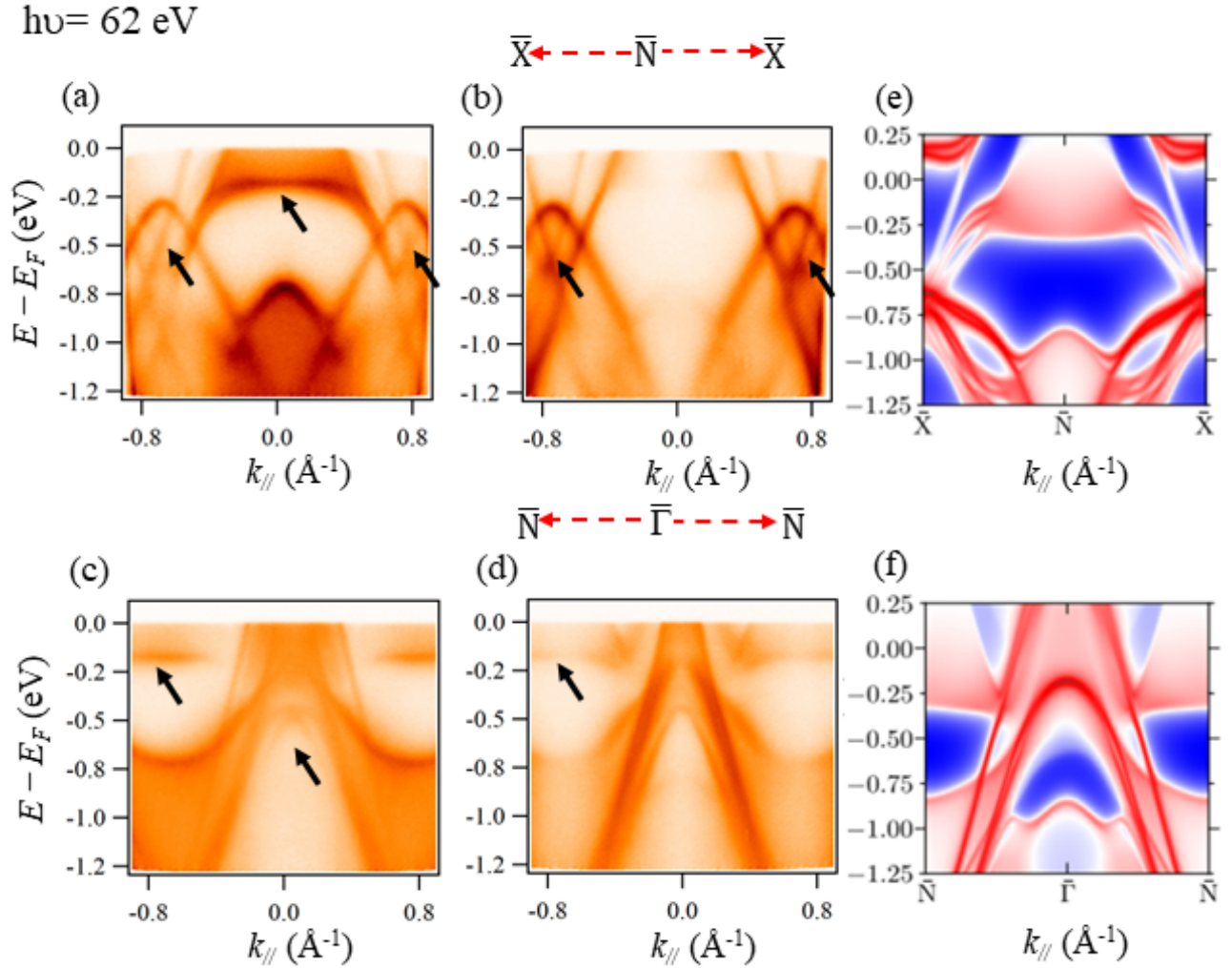


Fig. 3. Observation of flat bands and Dirac-like states in YRu_2Si_2 . **a** Experimental band dispersion along the \bar{X} - \bar{N} - \bar{X} direction using LH polarization and **b** LV polarization. **c** Experimental band dispersion along the \bar{N} - $\bar{\Gamma}$ - \bar{N} direction using LH polarization and **d** LV polarization. **e** DFT calculated band structure along the \bar{X} - \bar{N} - \bar{X} direction and **f** \bar{N} - $\bar{\Gamma}$ - \bar{N} direction. The black arrows indicate the Dirac-like states and flat bands. The experimental data were taken at the SSRL beamline 5-2 at a temperature of 15 K.

measurements as this band is strong in LH polarization and almost absent in LV polarization. The Dirac-like band at the \bar{X} point is quite intense in both LH and LV polarization measurements. In Fig. 3(c-d), we present the experimental band structure along the \bar{N} - $\bar{\Gamma}$ - \bar{N} direction. We observe flat bands at around 170 meV around the \bar{N} points for both the LH and LV polarizations. However, the intensity of the flat band is quite strong in LH polarization and weak in LV polarization. We also observe a Dirac-like structure at the $\bar{\Gamma}$ point at around 500 meV in LH polarization. The upper part of the Dirac-like structure at the $\bar{\Gamma}$ point is suppressed when the measurement is performed using LV polarization. The DFT calculated surface spectrum is presented in Fig. 3(e-f) and is in excellent agreement with the observed ARPES results. We have also performed orbital-resolved calculations to delineate the contribution of different orbitals and observed that the flat bands are strongly dominated by Ru $d_{x^2-y^2}$, Ru d_{xz} , and Ru d_{yz} orbitals [see Supplementary Note 3 and Supplementary Fig. 5 for orbital-resolved calculations]. The bulk Dirac-like band at the $\bar{\Gamma}$ point is composed of mainly Ru d_{z^2} orbitals with minor contribution from Ru d_{xz} orbitals. The density of states presented in Supplementary Note 3 and Supplementary Fig. 6 further shows that Ru d states predominantly contribute in the valence band region.

To further examine the dimensionality of the bands, we have performed photon energy dependent measurements along the \bar{X} - \bar{N} - \bar{X} direction using photon energies of 36 eV, 56 eV, and 68 eV using LH polarization as shown in Fig. 4. The flat bands are observed at around 170 meV for all the photon energies measured. The Dirac-like structure at the \bar{X} point is visible at the photon energies of 56 eV, 62 eV, and 68 eV [see Supplementary Note 4 and

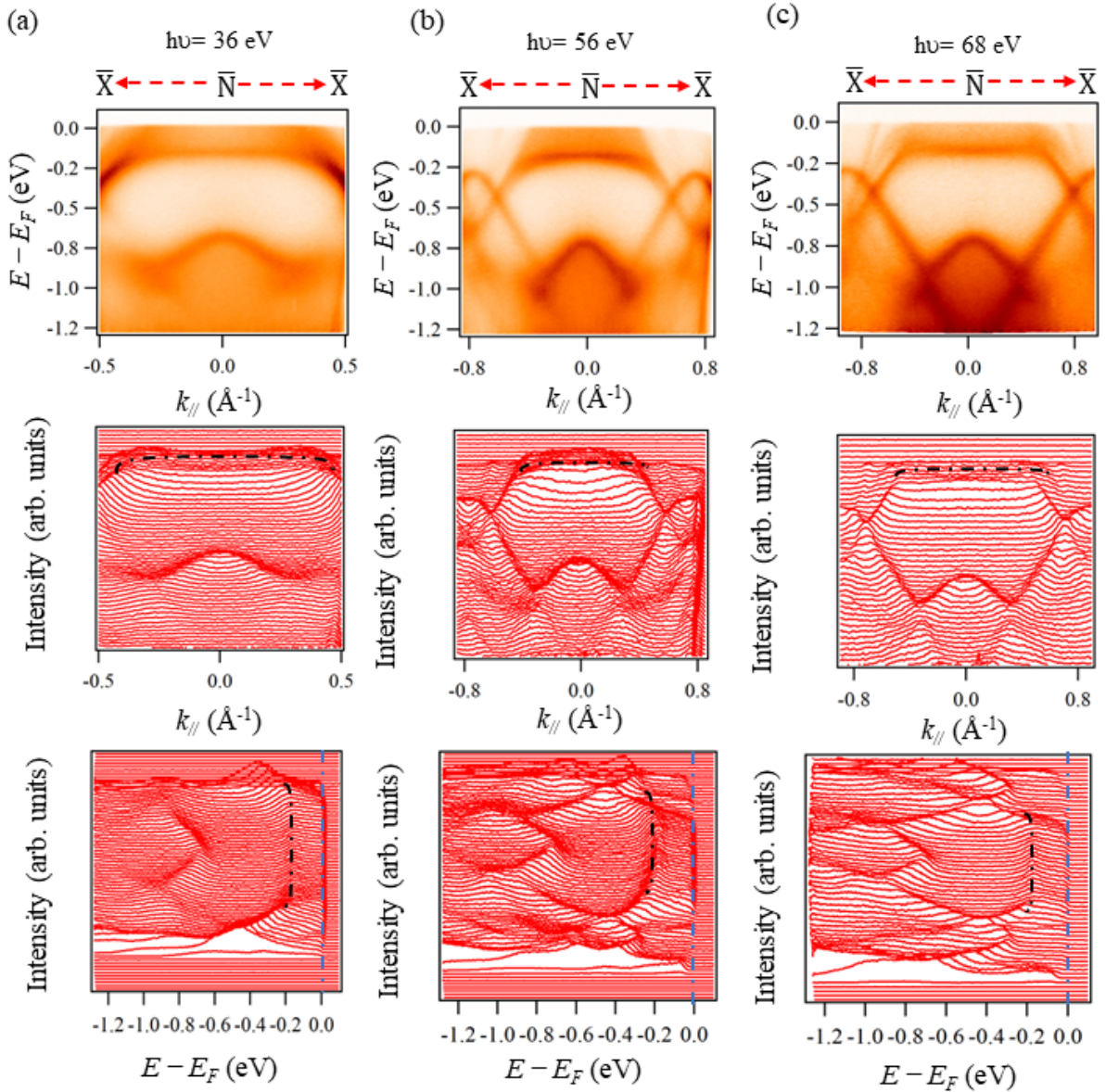


Fig. 4. Photon-energy dependent band dispersion along the \bar{X} - \bar{N} - \bar{X} direction. a-c Experimentally measured band dispersions along the \bar{X} - \bar{N} - \bar{X} direction using photon energies of **a** 36 eV, **b** 56 eV, and **c** 68 eV, respectively. The middle and the bottom panels are the momentum distribution curves (MDCs), and the energy distribution curves (EDCs) for the respective plots in **a-c**. The black dashed lines overlaid in the MDC plots are the hand-drawn curves showing the presence of flat bands for clarity and the blue dashed lines in EDCs represent the Fermi level. The experimental data were taken at the SSRL beamline 5-2 at a temperature of 15 K using LH polarization.

Supplementary Fig. 7a]. The momentum distribution curves (MDCs) and the energy distribution curves (EDCs) are presented in the middle and the bottom panel of Fig. 4(a-c), corresponding to their respective photon energies. The black dotted lines in both the MDCs and the EDCs confirm the non-dispersive flat bands in this material along the \bar{X} - \bar{N} - \bar{X} direction. The bands corresponding to hole pockets around the \bar{N} and a Dirac-like electron pocket at the \bar{X} point are evident in the figure. In Fig. 5 we present the polarization dependence of the bands observed along the \bar{N} - $\bar{\Gamma}$ - \bar{N} direction. The measurements have been performed at several photon energies using both LH and LV polarizations. The flat band at 170 meV can be seen in all the photon energies measured, however, the intensity of this flat band is more prominent at high photon energies and using LH polarization. This flat band, though still visible in LV polarization, seems to be suppressed quite strongly compared to LH polarization. The Dirac-like band observed at the $\bar{\Gamma}$ is visible in all the photon energies ranging from 66 eV to 108 eV using LH polarization [see Supplementary Note 4 and Supplementary Fig. 7b for zoomed in view of the Dirac-like states at the $\bar{\Gamma}$ point]. This

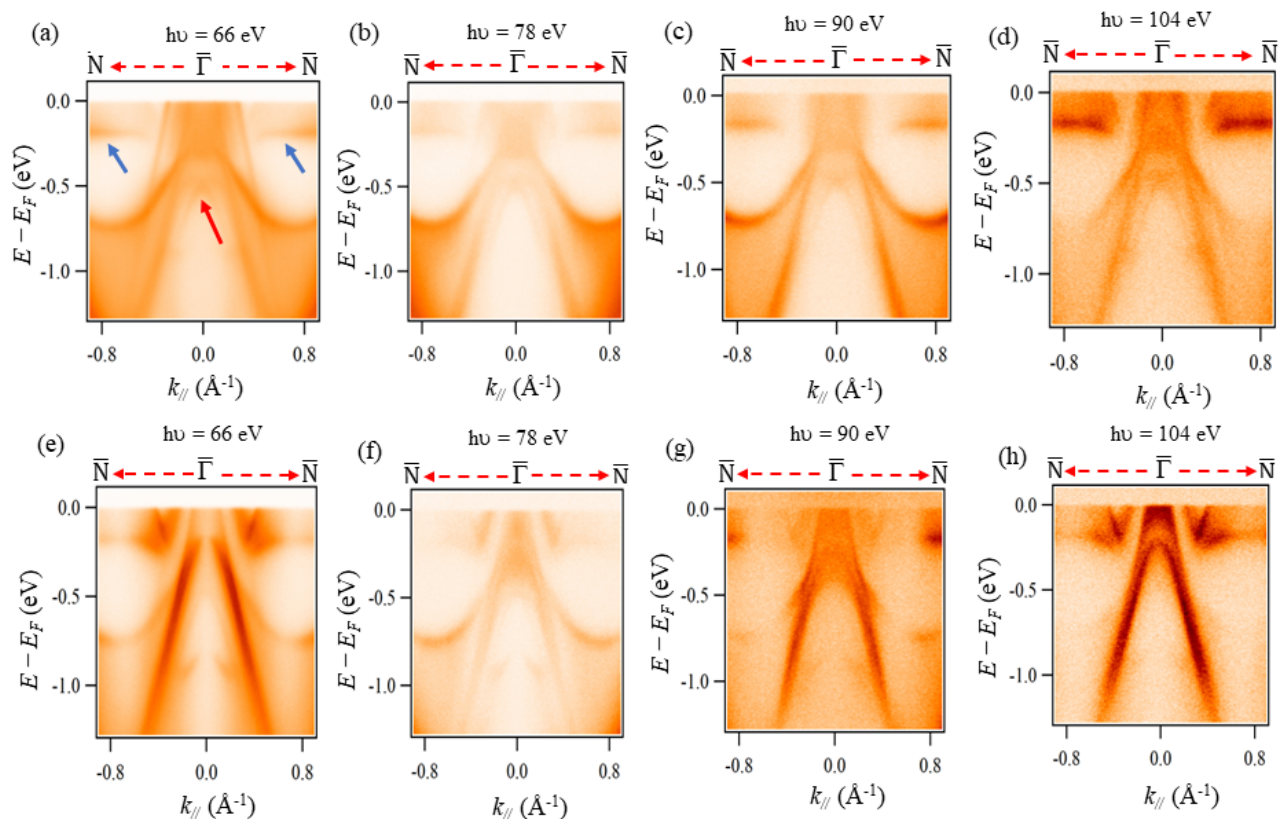


Fig. 5. Polarization dependent band dispersion along the $\bar{N}-\bar{\Gamma}-\bar{N}$ direction. Experimentally measured band dispersion along the $\bar{N}-\bar{\Gamma}-\bar{N}$ direction at various photon energies as indicated on top of the plots using **a-d** LH polarization and **e-h** LV polarization. The blue arrow shows the presence of flat bands and the red arrow shows Dirac-like bands at the $\bar{\Gamma}$ point. The experimental data were taken at the SSRL beamline 5-2 at a temperature of 15 K.

Dirac-like feature is visible at lower photon energies till 70 eV using LV polarization but is then strongly suppressed at higher photon energies and difficult to observe which may be due to its three-dimensional nature as well as the matrix element effect [46][see Supplementary Note 5 and Supplementary Fig. 8 for additional polarization dependent data at various photon energies]. The flat band at the \bar{N} point do not seem to change the dispersion as a function of photon energy, which suggests these bands essentially behave as two-dimensional in nature along the k_z direction also [see Supplementary Note 5 and Supplementary Fig. 8 for details]. The observation of the flat band and the Dirac-like band is in excellent agreement with our DFT calculated electronic structure as shown in the right hand side of Fig. 3c.

Discussion

In summary, we have studied the electronic structure of a new material YRu_2Si_2 using high-resolution ARPES and DFT calculations. This material is very interesting as it hosts flat bands within 170 meV along both the $\bar{N}-\bar{\Gamma}-\bar{N}$ and $\bar{X}-\bar{N}-\bar{X}$ high symmetry directions. These flat bands cover a large part of the BZ and is mainly contributed by Ru $d_{x^2-y^2}$, d_{xz} , and d_{yz} orbitals. In addition to this, YRu_2Si_2 also host 2D Dirac-like state at the \bar{X} point and a bulk 3D Dirac-like state at the $\bar{\Gamma}$ point. The bulk Dirac-like state at the $\bar{\Gamma}$ high-symmetry point is mainly contributed by Ru d_{z^2} orbitals. The obtained ARPES results are in excellent agreement with the DFT results. Our present electronic structure study of YRu_2Si_2 suggests that this material may provide an exciting platform for studying intriguing flat band physics in a weakly correlated material with negligible SOC (See Supplementary Fig. 9). To explore flat bands in condensed matter systems various materials such as kagome materials, and Moiré lattices have recently been the focus of interest. Observing flat bands in kagome materials have been challenging due to the strong electron-electron interactions present in these systems [28, 33, 34]. Moiré lattices serve as an excellent alternative to create flat bands artificially when two-dimensional materials stacked at a particular value of twist angle can result in flat bands forming close to the Fermi level thus resulting in strong electron-electron interactions and the formation of many-body states. However, precise manipulation of the twist angle in these Moiré lattices is a difficult task and defects, inhomogeneities, and environmental factors affect the reproducibility [47]. Our present study provides an exotic scenario where flat-band-like behavior can be observed in a weakly correlated material coexisting with

Dirac-like states. The flat bands can be further tuned by hole doping the system or gating so that it lies exactly at the Fermi level, which could give rise to ferromagnetism or superconductivity. Our discovery opens up a new research direction for the investigation of flat bands and non-trivial topology in weakly correlated systems with negligible SOC.

METHODS

Angle-resolved photoemission spectroscopy

ARPES measurements were performed at Stanford Synchrotron Radiation Lightsource (SSRL), endstation 5-2. Measurements were carried out at a temperature of 15 K. The pressure in the UHV was maintained better than 1×10^{-10} torr. The angular and energy resolution were set better than 0.2° and 15 meV, respectively. Measurements were performed employing the photon energies in the range of 30 eV-150 eV using both LH and LV polarizations. For details on experimental geometry see Ref. [48]

Theoretical calculations

DFT calculations were performed using the projector augmented-wave (PAW) potentials [49] implemented in the Vienna Ab initio Simulation Package [50–52]. Calculations are made within the generalized gradient approximation (GGA) in the Perdew, Burke, and Ernzerhof (PBE) parameterization [53]. The energy cutoff for the plane-wave expansion was set to 400 eV. In calculation we used the experimental lattice vectors as well as atomic positions [42]. The theoretically obtained Fermi level is overestimated with respect to the experimentally observed by around 0.2 eV. In our study, we present the theoretical results with the shifted Fermi level. The electronic band structure was also evaluated within Quantum ESPRESSO [54–56] with PSLIBRARY [57]. Exact results of the electronic band structure calculation, performed for primitive unit cell, was used to find the tight binding model in the basis of the maximally localized Wannier orbitals [58–60]. It was performed using the WANNIER90 software [61–63]. In our calculations, we used the $8 \times 8 \times 8$ full \mathbf{k} -point mesh, starting from the p orbitals of Si, while from the d and s orbitals for Y and Ru. Finally, 24-orbital tight binding model of YRu_2Si_2 , was used to investigate the surface Green's function for semi-infinite system [64], using WANNIERTOOLS [65] software.

Data availability

The data supporting the findings of this study are available within the paper, and other findings of this study are available from the corresponding author upon reasonable request.

REFERENCES

- [1] Li, Z. et al. Realization of flat band with possible nontrivial topology in electronic Kagome lattice. *Sci. Adv.* **4**, eaau4511 (2018).
- [2] Tokura, Y., Yasuda, K., Tsukazaki, A. Magnetic topological insulators. *Nat. Rev. Phys.* **1**, 126 (2019).
- [3] Derzhko, O., Richter, J., Maksymenko, M. Strongly correlated flat-band systems: The route from Heisenberg spins to Hubbard electrons. *Int. J. Mod. Phys. B* **29**, 1530007 (2015).
- [4] Bzdušek, T., Maciejko, J. Flat bands and band-touching from real-space topology in hyperbolic lattices. *Phys. Rev. B* **106**, 155146 (2022).
- [5] Aoki, H. Theoretical possibilities for flat band superconductivity. *J. Supercond. Nov. Magn.* **33**, 2341 (2020).
- [6] Tasaki, H. From Nagaoka's ferromagnetism to flat-band ferromagnetism and beyond: an introduction to ferromagnetism in the Hubbard model. *Prog. Theor. Phys.* **99**, 489 (1998).
- [7] Wu, C., Bergman, D., Balents, L. & Sarma, S. D. Flat Bands and Wigner Crystallization in the Honeycomb Optical Lattice. *Phys. Rev. Lett.* **99**, 070401 (2007).
- [8] Sheng, D., Gu, Z.-C., Sun, K. & Sheng, L. Fractional quantum Hall effect in the absence of Landau levels. *Nat. Commun.* **2**, 1-5 (2011).
- [9] Neupert, T., Santos, L., Chamon, C. & Mudry, C. Fractional quantum Hall states at zero magnetic field. *Phys. Rev. Lett.* **106**, 236804 (2011).
- [10] Sun, K., Gu, Z., Katsura, H. & Sarma, S. D. Nearly flatbands with nontrivial topology. *Phys. Rev. Lett.* **106**, 236803 (2011).
- [11] Tang, E., Mei, J.-W. & Wen, X.-G. High-temperature fractional quantum Hall states. *Phys. Rev. Lett.* **106**, 236802 (2011).
- [12] Regnault, N. & Bernevig, B. A. Fractional chern insulator. *Phys. Rev. X* **1**, 021014 (2011).
- [13] Parameswaran, S. A., Roy, R., Sondhi, & S. L. Fractional quantum Hall physics in topological flat bands. *C. R. Phys* **14**, 816 (2013).
- [14] Neupane, M. et al. Observation of a Novel Orbital Selective Mott Transition in $\text{Ca}_{1.8}\text{Sr}_{0.2}\text{RuO}_4$. *Phys. Rev. Lett.* **103**, 097001 (2009).

- [15] Neupane, M. et al. Surface electronic structure of the topological Kondo-insulator candidate correlated electron system SmB_6 . *Nat. Commun.* **4**, 2991 (2013).
- [16] Neupane, M. et al. Non-Kondo-like Electronic Structure in the Correlated Rare-Earth Hexaboride YbB_6 . *Phys. Rev. Lett.* **114**, 016403 (2015).
- [17] Asaba, T. et al. Colossal anomalous Nernst effect in a correlated noncentrosymmetric kagome ferromagnet. *Sci. Adv.* **7**, eabf1467 (2021).
- [18] Rao, Z., et al. Observation of unconventional chiral fermions with long Fermi arcs in CoSi . *Nature* **567**, 496 (2019).
- [19] Green, D., Santos, L. & Chamon, C. Isolated flat bands and spin-1 conical bands in two-dimensional lattices. *Phys. Rev. B* **82**, 075104 (2010).
- [20] Yin, J. X. et al. Negative flat band magnetism in a spin-orbit-coupled correlated kagome magnet. *Nat. Phys.* **15**, 443–448 (2019).
- [21] Kopnin, N. B., Heikkilä, T. T. & Volovik, G. E. High-temperature surface superconductivity in topological flat-band systems. *Phys. Rev. B* **83**, 220503(R) (2011).
- [22] Kopnin, N. B., Ijäs, M., Harju, A. & Heikkilä, T. T. High-temperature surface superconductivity in rhombohedral graphite. *Phys. Rev. B* **87**, 140503 (2013).
- [23] Marchenko, D. et al. Extremely flat band in bilayer graphene. *Sci. Adv.* **4**, 11 (2018).
- [24] Volovik, G. E. Graphite, graphene, and the flat band superconductivity. *JETP Lett.* **107**, 516–517 (2018).
- [25] Guo, H. M. & Franz, M. Topological insulator on the kagome lattice. *Phys. Rev. B* **80**, 113102 (2009).
- [26] Lin, Z. et al. Flatbands and emergent ferromagnetic ordering in Fe_3Sn_2 kagome lattices. *Phys. Rev. Lett.* **121**, 96401 (2018).
- [27] Ghimire, N. J. & Mazin, I. I. Topology and correlations on the kagome lattice. *Nat. Mater.* **19**, 137 (2020).
- [28] Kang, M. et al. Dirac fermions and flat bands in the ideal Kagome metal FeSn . *Nat. Mater.* **19**, 163–169 (2020).
- [29] Kang, M. et al. Topological flat bands in frustrated kagome lattice CoSn . *Nat. Commun.* **11**, 4004 (2020).
- [30] Li, M. et al. Dirac cone, flat band and saddle point in kagome magnet YMn_6Sn_6 . *Nat. Commun.* **12**, 3129 (2021).
- [31] Regmi, S. et al. Spectroscopic evidence of flat bands in breathing kagome semiconductor Nb_3I_8 . *Commun Mater* **3**, 100 (2022).
- [32] Yilmaz, T. et al. Emergent flat band electronic structure in a $\text{VSe}_2/\text{Bi}_2\text{Se}_3$ heterostructure. *Commun Mater* **2**, 11 (2021).
- [33] Dhakal, G. et al. Anisotropically large anomalous and topological Hall effect in a kagome magnet. *Phys. Rev. B* **104**, L161115 (2021).
- [34] Kabir, F. et al. Unusual magnetic and transport properties in HoMn_6Sn_6 kagome magnet. *Phys. Rev. Mater.* **6**, 064404 (2022).
- [35] Henni, Y. et al. Rhombohedral multilayer graphene: A magneto-Raman scattering study. *Nano Lett.* **16**, 3710–3716 (2016).
- [36] Pierucci, D. et al. Evidence for Flat Bands near the Fermi Level in Epitaxial Rhombohedral Multilayer Graphene. *ACS nano* **9**, 5432–5439 (2015).
- [37] Pamuk, B., Baima, J., Mauri, F. & Calandra, M. Magnetic gap opening in rhombohedral-stacked multilayer graphene from first principles. *Phys. Rev. B* **95**, 075422 (2017).
- [38] Henck, H. et al. Flat electronic bands in long sequences of rhombohedral-stacked graphene. *Phys. Rev. B* **97**, 245421 (2018).
- [39] Bistritzer, R. & MacDonald, A. H. Moiré bands in twisted double-layer graphene. *Proc. Natl. Acad. Sci. U.S.A.* **108**, 12233–12237 (2011).
- [40] Cao, Y. et al. Unconventional superconductivity in magic-angle graphene superlattices. *Nature* **556**, 43–50 (2018).
- [41] Ehlen, N. et al. Origin of the Flat Band in Heavily Cs-Doped Graphene. *ACS Nano* **14**, 1055–1069 (2020).
- [42] Höting, C., Eckert, H., Matar, S. F., Rodewald, U. C. & Pöttgen, R. The Silicides YT_2Si_2 ($T = \text{Co, Ni, Cu, Ru, Rh, Pd}$): A Systematic Study by ^{89}Y Solid-state NMR Spectroscopy. *Zeitschrift für Naturforschung B* **69**, 305–312 (2014).
- [43] Inoue, D. et al. Thermal Expansion and Magnetostriction of Heavy Fermion CeRu_2Si_2 at Millikelvin Temperatures. *Physics Procedia* **75**, 158–165 (2015).
- [44] Settai, R. et al. Fermi surfaces of YRu_2Si_2 and LaRu_2Si_2 . *Physica B Condens. Matter* **206–207**, 23–25 (1995).
- [45] Ikezawa, H. et al. Magnetoresistance and de Haas-van Alphen Effect in YRu_2Si_2 . *J. Phys. Soc. Jpn.* **64**, 3422–3428 (1995).
- [46] Sakhya, A. P. et al. Behavior of gapped and ungapped Dirac cones in the antiferromagnetic topological metal SmBi . *Phys. Rev. B* **106**, 085132 (2022).
- [47] Lau, C. N., Bockrath, M. W., Mak, K. F. & Zhang, F. Reproducibility in the fabrication and physics of moiré materials. *Nature* **602**, 41–50 (2022).
- [48] Regmi, S. et al. Observation of gapless nodal-line states in NdSbTe . *arXiv preprint arXiv:2210.00163* (2022).
- [49] Blöchl, P. E. Projector augmented-wave method. *Phys. Rev. B* **50**, 17953–17979 (1994).
- [50] Kresse, G. & Hafner, J. Ab initio molecular-dynamics simulation of the liquid-metal–amorphous-semiconductor transition in germanium. *Phys. Rev. B* **49**, 14251–14269 (1994).
- [51] Kresse, G. & Furthmüller, J. Efficient iterative schemes for ab initio total-energy calculations using a plane-wave basis set. *Phys. Rev. B* **54**, 11169–11186 (1996).
- [52] Kresse, G. & Joubert, D. From ultrasoft pseudopotentials to the projector augmented-wave method. *Phys. Rev. B* **59**, 1758–1775 (1999).
- [53] Perdew, J. P., Burke, K. & Ernzerhof, M. Generalized Gradient Approximation Made Simple. *Phys. Rev. Lett.* **77**, 3865–3868 (1996).
- [54] Giannozzi, P. et al. QUANTUM ESPRESSO: a modular and open-source software project for quantum simulations of materials. *J. Phys. Condens. Matter.* **21**, 395502 (2009).
- [55] Giannozzi, P. et al. Advanced capabilities for materials modelling with Quantum ESPRESSO. *J. Phys. Condens. Matter.*

- 29**, 465901 (2017).
- [56] Giannozzi, P. et al. Quantum ESPRESSO toward the exascale. *J. Chem. Phys.* **152**, 154105 (2020).
 - [57] Dal Corso, A. Pseudopotentials periodic table: From H to Pu. *Comput. Mater. Sci.* **95**, 337-350 (2014).
 - [58] Marzari, N., Mostofi, A. A., Yates, J. R., Souza, I. & Vanderbilt, D. Maximally localized Wannier functions: Theory and applications. *Rev. Mod. Phys.* **84**, 1419-1475 (2012).
 - [59] Marzari, N. & Vanderbilt, D. Maximally localized generalized Wannier functions for composite energy bands. *Phys. Rev. B* **56**, 12847-12865 (1997).
 - [60] Souza, I., Marzari, N. & Vanderbilt, D. Maximally localized Wannier functions for entangled energy bands. *Phys. Rev. B* **65**, 035109 (2001).
 - [61] Mostofi, A. A. et al. wannier90: A tool for obtaining maximally-localised Wannier functions. *Comput. Phys. Commun.* **178**, 685-699 (2008).
 - [62] Mostofi, A. A. et al. An updated version of wannier90: A tool for obtaining maximally-localised Wannier functions. *Comput. Phys. Commun.* **185**, 2309-2310 (2014).
 - [63] Pizzi, G. et al. Wannier90 as a community code: new features and applications. *J. Phys. Condens. Matter.* **32**, 165902 (2020).
 - [64] Sancho, M. L., Sancho, J. L., Sancho, J. L. & Rubio, J. Highly convergent schemes for the calculation of bulk and surface Green functions. *Journal of Physics F: Metal Physics* **15**, 851 (1985).
 - [65] Wu, Q., Zhang, S., Song, H.-F., Troyer, M. & Soluyanov, A. A. WannierTools: An open-source software package for novel topological materials. *Comput. Phys. Commun.* **224**, 405-416 (2018).

ACKNOWLEDGMENTS

M.N. acknowledges the support by the Air Force Office of Scientific Research MURI (Grant No. FA9550-20-1-0322), and the National Science Foundation (NSF) CAREER award DMR-1847962. A.P. acknowledges the support by National Science Centre (NCN, Poland) under Projects No. 2021/43/B/ST3/02166 and also appreciates the funding in the frame of scholarships of the Minister of Science and Higher Education (Poland) for outstanding young scientists (2019 edition, No. 818/STYP/14/2019). The use of Stanford Synchrotron Radiation Lightsource (SSRL) in SLAC National Accelerator Laboratory is supported by the U.S. Department of Energy, Office of Science, Office of Basic Energy Sciences under Contract No. DE-AC02-76SF00515. We thank Makoto Hashimoto and Donghui Lu for the beamline assistance at SSRL endstation 5-2.

ADDITIONAL INFORMATION

Correspondence and requests for materials should be addressed to Madhab Neupane.